

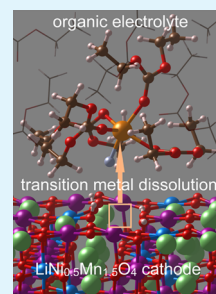
# Ab Initio Modeling of Transition Metal Dissolution from the $\text{LiNi}_{0.5}\text{Mn}_{1.5}\text{O}_4$ Cathode

Nadia N. Intan,<sup>†</sup> Konstantin Klyukin,<sup>†,||</sup> and Vitaly Alexandrov<sup>\*,†,‡,||</sup>

<sup>†</sup>Department of Chemical and Biomolecular Engineering and <sup>‡</sup>Nebraska Center for Materials and Nanoscience, University of Nebraska–Lincoln, Lincoln, Nebraska 68588, United States

**ABSTRACT:** Irreversible dissolution of transition metals (TMs) from cathode materials in lithium-ion batteries (LIBs) represents a serious challenge for the application of high-energy-density LIBs. Despite substantial improvements achieved by Ni doping of the  $\text{LiMn}_2\text{O}_4$  spinel, the promising high-voltage  $\text{LiNi}_{0.5}\text{Mn}_{1.5}\text{O}_4$  (LNMO) cathode material still suffers from the loss of electro-active materials (Mn and Ni). This process contributes to the formation of solid–electrolyte interfaces and capacity loss severely limiting the battery life cycle. Here, we combine static and ab initio molecular dynamics free energy calculations based on the density functional theory to investigate the mechanism and kinetics of TM dissolution from LNMO into the liquid organic electrolyte. Our calculations help deconvolute the impact of various factors on TM dissolution rates such as the presence of surface protons and oxygen vacancies and the nature of TMs and electrolyte species. The present study also reveals a linear relationship between adsorption strength of the electrolyte species and TM dissolution barriers that should help design electrode/electrolyte interfaces less vulnerable to TM dissolution.

**KEYWORDS:** *ab initio molecular dynamics, transition-metal dissolution, lithium-ion battery, spinel cathode, solid–electrolyte interface*



## 1. INTRODUCTION

Lithium-ion battery (LIB) cathode materials can undergo diverse electrochemically driven degradation processes causing irreversibility upon intercalation/deintercalation of Li ions. This includes phase transformations, structural disorder, decomposition of the organic electrolyte, and dissolution of transition metals (TMs). It is well established experimentally that active metal dissolution is a common phenomenon across LIB oxide-based cathodes regardless of their crystal structure and chemical composition.<sup>1–5</sup> Despite a clear correlation between dissolution of TM ions and capacity fading of the cell established in experiments across a variety of cathode materials,<sup>4,5</sup> our microscopic understanding of TM dissolution is still insufficient. Mechanistic insights into TM dissolution are hampered by the complexity of electrode/electrolyte interfaces with a dynamic coupling between a variety of interfacial processes making interpretation of experimental observations rather challenging.

Among LIB cathode materials, spinel-structured  $\text{LiNi}_{0.5}\text{Mn}_{1.5}\text{O}_4$  (LNMO) has attracted a lot of attention as a promising high-voltage cathode compound ( $\sim 4.7$  V vs  $\text{Li}/\text{Li}^+$ ).<sup>4,6</sup> Compared to the  $\text{LiMn}_2\text{O}_4$  (LMO) spinel, LNMO is characterized by improved stability including less pronounced TM dissolution owing to Ni doping, which stabilizes Mn(IV) in the crystal lattice.<sup>7,8</sup> Although introduction of Ni by partial substitution of Mn has decreased the amount of dissolved Mn, complete suppression of Mn dissolution from LNMO cannot be achieved.<sup>4,5</sup> In addition, dissolution of Ni is observed, albeit in lesser amounts than that of Mn.

Hunter's disproportionation reaction  $2\text{Mn(III)} \rightarrow \text{Mn(II)} + \text{Mn(IV)}$  is believed to play an important role in generating

Mn(II) species prone to dissolution. However, recent experimental studies of both LMO and LNMO demonstrated that the Mn(II) concentration at the cathode surface is also high at the fully charged state that is expected to suppress the disproportionation reaction.<sup>4,10</sup> This was attributed to the key role of cathode–electrolyte surface reactions triggering Mn(II) formation and dissolution. Overall, it is recognized that the cathode surface becomes more oxidative upon delithiation promoting protonation of surface oxygen atoms, weakening Mn–O bonds, and facilitating Mn dissolution; however, the mechanisms of TM release and migration to the anode are not completely understood. For example, a fluorescence spectroscopy-based investigation of LNMO identified specific organic fragments such as  $\beta$ -diketonate produced from the diethyl carbonate (DEC) solvent, which were suggested to strongly bind to surface Mn by forming bidentate complexes via C–O groups and thus promote facile Mn dissolution.<sup>11</sup> However, whether this mechanism is operative or such complexes only form in the electrolyte at later stages remains unclear.

Previous density functional theory (DFT) computational studies were carried out considering Mn dissolution from LMO in either aqueous<sup>12</sup> or the ethylene carbonate (EC) electrolyte<sup>13</sup> solutions and provided important atomistic insights into the plausible scenarios of Mn release. For example, it was demonstrated that even a small displacement of Mn(III) from the equilibrium lattice site of the LMO surface results in its reduction to Mn(II) in both aqueous and EC

Received: April 5, 2019

Accepted: May 13, 2019

Published: May 13, 2019

environments.<sup>12,13</sup> It was suggested that once disproportionation has occurred, Mn(II) will most likely dissolve rather than reattach to the surface. It was also reported based on DFT calculations that EC molecules will decompose and protonate the LMO surfaces promoting Mn dissolution.<sup>13–15</sup> Theoretical studies of LNMO are more scarce and primarily address the bulk properties of the LNMO spinel rather than the cathode–electrolyte interfacial behavior.<sup>16–18</sup>

The purpose of this study is twofold. First, we aim to carry out a systematic computational investigation of Mn and Ni dissolution from the LNMO spinel providing microscopic information about the TM dissolution mechanism and deconvoluting the influence of several factors on dissolution barriers. Second, we attempt to establish a relationship between the electrode/electrolyte chemistry and cathode stability that can be used more generally to predict the propensity of cathode materials to TM dissolution. To this end, we apply ab initio molecular dynamics (AIMD)-based rare event simulations combined with static DFT calculations of the LNMO/electrolyte interface. The remainder of this paper is organized as follows. First, computational methodology and details of the simulations are described. Then, we present the obtained results along with the discussion of the dissolution reaction mechanism and associated free energy barriers of TM dissolution. Finally, we correlate the adsorption strength of the electrolyte species on TM to the dissolution free energy barriers, which allows us to predict TM dissolution behavior based solely on static DFT calculations of adsorption energies.

## 2. COMPUTATIONAL METHODS

LNMO can display two different Ni/Mn arrangements depending on synthesis conditions: Ni/Mn ordered (space group  $P4_332$ ) and disordered (space group  $Fd\bar{3}m$ ) cubic phases.<sup>18,19</sup> It was demonstrated that the ordered phase is more energetically favorable than the disordered phase. The surfaces of ordered LNMO nanoparticles are known to be primarily truncated by the (001) and (111) facets,<sup>20</sup> with Li termination of the (001) surface exhibiting the lowest surface energy.<sup>21–24</sup> The (001) lithiated LNMO surface was modeled within a periodic slab model composed of four LNMO layers, a vacuum gap of 10 Å, and an extended surface cell, resulting in an  $11.57 \times 11.57 \times 20.20$  Å<sup>3</sup> simulation cell. The vacuum gap was filled by 8 DEC molecules (see Figure 1). Inorganic species (fluorine and protons) were added into the system without modifying the number of DEC molecules, while other carbonate-based organic molecules were introduced by substituting one of the eight DEC molecules. All calculations were carried out using a neutral simulation cell. TMs (Mn, Ni) at the (001) surface are coordinated by five oxygen atoms depicted in Figure 1 as  $O_{\text{sub}}$  (subsurface),  $O_{3f}$  (3-fold-coordinated), and  $O_{2f}$  (2-fold-coordinated).

All calculations were performed using the Vienna ab initio simulation package (VASP)<sup>25,26</sup> within the projector augmented-wave (PAW) approach.<sup>27</sup> Generalized gradient approximation Perdew–Burke–Ernzerhof (PBE) exchange–correlation functional<sup>28</sup> was employed in the modified form for solids PBEsol,<sup>29</sup> which was used in combination with DFT-D3 Grimme to account for long-range van der Waals interactions.<sup>30</sup> The Li, Mn<sub>pv</sub>, O<sub>s</sub>, Ni, C<sub>s</sub>, H, and F potentials (1, 13, 6, 10, 4, 1, and 7 valence electrons, respectively) were chosen from the VASP PBE-PAW library. Antiferromagnetic ordering was imposed on Ni and Mn in accordance with experiments.<sup>31,32</sup> The rotationally invariant Hubbard-type correction was adopted with  $U_{\text{eff}} = 3.9$  and 6.0 eV on the Mn and Ni 3d orbitals, respectively.<sup>24</sup> The evolution of the oxidation state of both manganese and nickel was monitored through the changes in its magnetic moment. Mn(II), Mn(III), and Mn(IV) were distinguished by net spins of  $\sim 4.4$ ,  $\sim 3.8$ , and  $\sim 3.2$   $\mu_B$ , respectively,<sup>13</sup> while net spins of

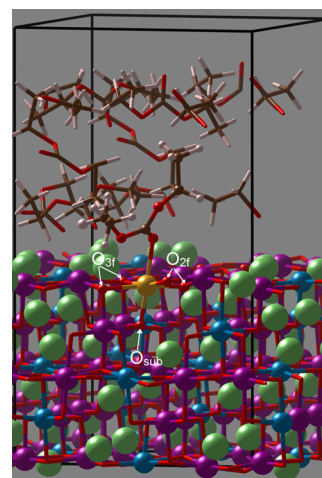


**Figure 1.** Simulation cell used to model TM dissolution from the (001) LNMO surface. The dissolving TM atom is depicted in orange, while Li, Ni, Mn, O, C, and H atoms are depicted in green, blue, magenta, red, brown, and white, respectively. The three types of O atoms in the first coordination sphere of TM (subsurface  $O_{\text{sub}}$ , surface 2-fold  $O_{2f}$ , and 3-fold  $O_{3f}$ -coordinated) are also indicated.

$\sim 1.6$  and  $\sim 0.9$   $\mu_B$  were used to differentiate between Ni(II) and Ni(III) ions.<sup>33</sup> Static calculations were done with a  $2 \times 2 \times 1$   $k$ -point mesh until the atomic forces were converged to less than 0.02 eV/Å. The adsorption energy was calculated using the following equation:  $E_{\text{ads}} = E(\text{slab} + \text{adsorbate}) - E(\text{slab}) - E(\text{adsorbate})$ .

Dissolution modeling was performed within the Born–Oppenheimer molecular dynamics methodology. The systems under study were initially equilibrated during 10 ps using a time step of  $\delta t = 1$  fs with all hydrogen atoms replaced with deuterium. The Nose–Hoover thermostat<sup>34,35</sup> was used to keep the simulation temperature around 300 K. Slow-growth approach<sup>36</sup> with a velocity of 0.5 Å/ps was employed to explore the TM dissolution pathway. Each TM–O bond breaking event was sampled separately using the slow-growth approach with the bond distance between the dissolving TM and oxygen atom specific to each reaction step chosen as the collective variable (CV).<sup>37</sup>

The blue moon ensemble approach<sup>38</sup> was employed to explore the free energy landscape of the dissolution process. Each slow-growth trajectory was split into a set of windows with a spacing of  $\sim 0.1$  Å, and atomic configuration in each window was then equilibrated for 2 ps. Each equilibration was followed by 2 ps of production run to collect force gradients along the constrained reaction coordinate. Finally, the free energy profile was calculated through thermodynamic integration of the averaged force gradients along the reaction path. A similar approach has been recently employed in the dissolution studies of LMO<sup>12,13</sup> and other materials.<sup>39</sup>

## 3. RESULTS AND DISCUSSION

Complete dissolution of TMs from the ideal (100) LNMO surface into the electrolyte solution requires breaking of all the five TM–O bonds (see Figure 1) characterized by several metastable states with the corresponding activation barriers. We start our analysis by considering partial release of Ni/Mn from the pristine LNMO surface to the surface-bound configuration. For this dissolution step, we identify the reaction mechanism and analyze the impact of various factors on dissolution barriers such as protonation state of the cathode surface, the role of oxygen defects, and electrolyte species. Then, we consider dissolution of TMs from the surface-bound configuration into the electrolyte solution. On the basis of the obtained results, we establish a correlation between the

magnitude of TM dissolution barriers and adsorption strength of the electrolyte species.

**3.1. Partial Release of TM to the Surface-Bound Configuration.** In this section, we analyze dissolution of Ni/Mn from the LNMO surface to the surface-bound configuration. To unveil the dissolution mechanism, we employ the slow-growth approach choosing the  $\text{Mn}-\text{O}_{\text{sub}}$  bond distance as a CV similar to a previous DFT study of Mn dissolution from LMO.<sup>13</sup> Figure 2a shows the evolution of the  $\text{Mn}-\text{O}$

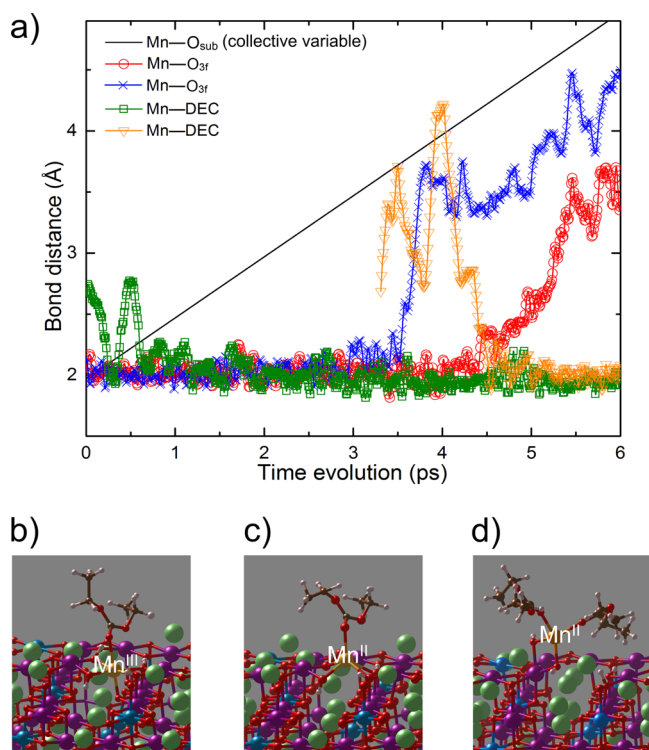


**Figure 2.** (a) Representative trajectory of Mn partial release from the LNMO surface to the above-surface position. The sequence of bond-breaking and bond-making events is obtained from slow-growth simulations with the  $\text{Mn}-\text{O}_{\text{sub}}$  distance as the CV. (b) Initial configuration; (c) intermediate configuration showing breaking of the  $\text{Mn}-\text{O}_{\text{sub}}$  bond and the reduction of Mn(III) to Mn(II); (d) final configuration where the dissolving TM is located above the LNMO surface and forms a tetrahedral complex with two electrolyte molecules. Li, Ni, Mn, O, C, and H atoms are depicted in green, blue, magenta, red, brown, and white, respectively. For clarity, extra DEC molecules in electrolyte are removed, while the dissolving TM atom is depicted in orange.

bond distances upon increasing the CV, revealing a sequence of bond-breaking and bond-forming events during dissolution. The overall sequence of events identified by these slow-growth simulations is found to be the same for Mn and Ni, which agrees well with previous theoretical studies of Mn dissolution from LMO into water<sup>12</sup> or EC electrolyte.<sup>13</sup>

The atomic structures of dissolving Mn at the initial, intermediate, and final states are shown in Figure 2b-d. It is seen that Mn dissolution starts with a single DEC molecule adsorbed at the surface Mn(III) ion via the  $\text{C}=\text{O}$  group. Upon breaking of the  $\text{Mn}-\text{O}_{\text{sub}}$  bond as depicted in Figure 2c, Mn gets reduced from Mn(III) to Mn(II), in agreement with the LMO case.<sup>12,13</sup> Further increase of the  $\text{Mn}-\text{O}_{\text{sub}}$  CV leads to a consecutive breaking of the two  $\text{Mn}-\text{O}_{3f}$  bonds that are weaker than  $\text{Mn}-\text{O}_{2f}$ . The breaking of the third  $\text{Mn}-\text{O}$

enables a second DEC molecule to form a bond with dissolving Mn(II), as shown in Figure 2d. Thus, in its final configuration, the surface-bound TM forms a stable tetrahedral complex with two DEC molecules and two surface  $\text{O}_{2f}$  atoms. These simulations also reveal that the TM release to the surface is coupled to Li diffusion from the interior of the slab to the TM vacancy site left behind by the dissolving TM. It is found that this Li diffusion stabilizes the reaction intermediate and lowers the free energy barrier of TM dissolution by 0.2 eV relative to the delithiated surface where no Li is available to fill the TM vacancy site. Such Li-ion diffusion should also contribute to the irreversibility of TM dissolution.

We next analyze the kinetics of TM dissolution, and Figure 3 shows the exemplary blue moon free energy profiles of Mn release from the LNMO surface for two cases. Figure 3a depicts Mn dissolution in the ideal case of the pristine LNMO surface and DEC electrolyte, whereas Figure 3b demonstrates a dramatic role of surface protonation and the presence of  $\text{F}^-$  in the electrolyte on the magnitude of the dissolution barrier. The formation of a stable surface-bound Mn intermediate is considered to be complete when the free energy is plateaued at the CV value of about 5.0 Å, consistent with the LMO investigation.<sup>13</sup> The binding of the third DEC molecule is sterically hindered at the surface, while smaller electrolyte species such as  $\text{F}^-$  may bind to the dissolving Mn ion. To provide a more systematic insight into how electrode/electrolyte interfacial chemistry may affect dissolution, below we analyze the influence of surface protonation, the nature of electrolyte species, as well as the presence of a surface oxygen vacancy on the dissolution barriers for both Mn and Ni in detail.

It is well established that protons can be generated in the working environment of LIBs, for example, through decomposition of the organic electrolyte species,<sup>14</sup> dissociation of water,<sup>40</sup> and hydrofluoric acid (HF) formed at high temperatures because of the interaction between the battery electrolyte counterions  $\text{PF}_6^-$  and traces of  $\text{H}_2\text{O}$  in the electrolyte.<sup>41</sup> For example, it was demonstrated that the amounts of dissolved Mn and Ni increase with temperature, which correlates well with more rapid hydrolysis of  $\text{LiPF}_6$  at elevated temperatures to yield HF protonating the surface.<sup>4</sup> The formed  $\text{F}^-$  anions can also strongly bind to the surface TM ions, facilitating the dissolution process. Table 1 summarizes the free energy barriers estimated for both Mn and Ni distinguishing the effects of surface protonation,  $\text{F}^-$  binding, and the presence of oxygen vacancy in the vicinity of the dissolving TM in the DEC environment.

We find that protonation of the  $\text{O}_{2f}$  surface sites does not significantly affect the activation barrier, in agreement with the fact that  $\text{TM}-\text{O}_{2f}$  bonds do not break during this first dissolution step as observed in slow-growth simulations (Figure 1). Protonation of the  $\text{O}_{3f}$  sites, on the other hand, results in a substantial reduction of the TM dissolution barriers. This is because protonation weakens surface  $\text{TM}-\text{O}$  bonds and also contributes to the reduction of  $\text{Mn}^{2+}$  promoting dissolution. It is seen from the table that protonation of all four oxygen atoms neighboring the dissolving Mn ion reduces the activation barrier by almost 1 eV with respect to the pristine surface case. As compared to Mn, Ni is characterized by smaller (by  $\sim 0.3$ – $0.4$  eV) dissolution barriers than Mn. This is in general agreement with experimental investigations demonstrating considerable dissolution of both Mn and Ni from LNMO surfaces.<sup>4</sup> The

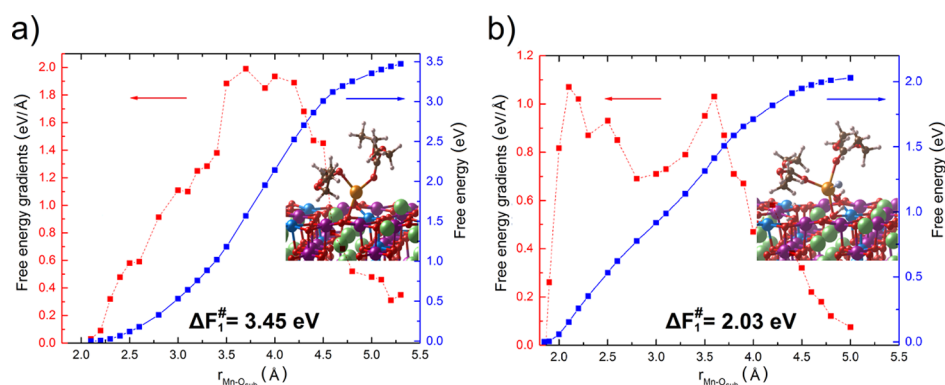


**Figure 3.** Averaged free energy gradients (left axis) and the corresponding free energy profiles (right axis) of Mn partial release to the surface-bound state are shown as estimated in blue moon simulations: (a) from pristine LNMO surface, leading to the formation of Mn intermediates with two DEC molecules, and (b) from LNMO surface where all four surface oxygen atoms neighboring the dissolving Mn are protonated, leading to the formation of a stable Mn intermediate with two DEC molecules and one  $F^-$  anion (shown in light blue).

**Table 1.** Free Energy Barriers of Mn/Ni Partial Release from the LNMO Surface to the Surface-Bound Configuration in the DEC Electrolyte ( $\Delta F_1^\ddagger$ )<sup>a</sup>

system	$\Delta F_1^\ddagger$ (eV)	
	Mn	Ni
pristine LNMO	3.45	
4H/LNMO	2.68	2.37
4H/LNMO + 1 $F^-$	2.03	1.62
4H/LNMO + 1 $F^-$ + 1 $V_O$	1.61	
4H/LNMO + 2 $F^-$	1.4	1.3

<sup>a</sup>4H/LNMO denotes the case in which four oxygen atoms adjacent to the dissolving TM are protonated. 1 $F^-$  and 2 $F^-$  stand for the cases with one or two fluorine ions attached to the dissolving TM, while 1 $V_O$  corresponds to the creation of one surface oxygen vacancy in the immediate vicinity of the dissolving TM.

relative amounts of dissolved Mn and Ni were determined to vary depending on experimental conditions being affected by morphological and chemical inhomogeneities.<sup>4</sup> The obtained computational results are consistent with experiments showing more pronounced TM dissolution at the charged state.<sup>4</sup> The charge compensation by protons suggests that the degree of LNMO surface protonation directly correlates with the state of charge of the battery,<sup>42</sup> and thus, materials at the delithiated state should be more prone to dissolution.

Dissociation products of inorganic salts such as  $LiPF_6$ ,  $LiBF_4$ , and  $LiClO_4$  present in the organic electrolyte are known to play a crucial role in the stability of electrodes and TM dissolution can be significantly reduced by varying the type of inorganic salt.<sup>43,44</sup> In the case of  $LiPF_6$  or  $LiBF_4$  in the carbonate-based electrolyte, significant amounts of metal fluorides such as  $LiF$ ,  $MnF_2$ , and  $NiF_2$  are detected in the cathode–electrolyte interface (CEI) layer causing capacity fading.<sup>4</sup> Here, we analyze the role of  $F^-$  ions from  $PF_6^-$  decomposition<sup>45,46</sup> on the TM dissolution kinetics. As seen from Table 1, a single  $F^-$  ion bound to the dissolving TM species leads to a substantial reduction of the dissolution barrier by  $\sim 0.7$ – $0.8$  eV as compared to the DEC case. If two  $F^-$  ions participate in the dissolution reaction, the barrier is reduced by another 0.5 (0.3) eV for Mn (Ni). Note that the second  $F^-$  ion can only bind to the dissolving TM after the  $TM-O_{sub}$  bond breaks at around 3 Å.

Another critical factor that should affect TM dissolution rates is the presence of surface oxygen vacancies formed during

either electrode synthesis or LIB operation (e.g., through protonation of surface oxygen atoms to yield  $H_2O$ ).<sup>4,11,40</sup> Because the weakening of the  $TM-O_{3f}$  bond should have a more pronounced impact on the dissolution barrier, we created an oxygen vacancy at the  $O_{3f}$  site. We find that the presence of a single vacancy lowers the free energy barrier for Mn partial release by  $\sim 0.4$  eV, resulting in a value of 1.61 eV for the single  $F^-$  case. It is thus expected that if TM dissolution is considered for the most favorable case with one oxygen vacancy  $V_O$  and two  $F^-$  at the LNMO surface, the rate of Mn dissolution corresponding to the barrier of 1.0 eV using a common kinetic prefactor of  $10^{12} s^{-1}$  can be reasonably estimated as  $\sim 22$  h at room temperature. It should be noted, however, that quantitative comparison of dissolution rates between theory and experiments is problematic because the rates are extremely sensitive to computationally predicted values of the dissolution barrier, whereas accurate dissolution-rate experiments are plagued with side processes such as the buildup of the CEI layer that can retard dissolution reactions. Simulations also indicate that Ni has systematically lower dissolution barriers than Mn (Table 1), while higher concentrations of dissolved Mn than Ni are detected experimentally for LNMO.<sup>4</sup> This could be partially explained by the higher content of Mn in LNMO (3:1).

In a recent experimental study of TM dissolution from the LNMO cathode,<sup>11</sup> it was postulated based on the observed TM complexes that  $\beta$ -diketonate ligands generated upon anodic oxidation of EC and DEC may chelate surface TMs and facilitate their dissolution to the electrolyte. The reaction was hypothesized to occur through a sequence of interfacial proton-coupled electron-transfer processes involving a heterolytic C–H bond cleavage, protonation of surface O atoms to yield water, and the formation and desorption of a surficial Mn(III) bidentate  $\beta$ -diketonate coordination complex. To provide some insights into the plausibility of this mechanism, here we examine the energetics of TM release as a bidentate  $\beta$ -diketonate metal complex without examining the actual mechanism and kinetics of formation of  $\beta$ -diketonate chelate ligands at the interface. To this end, we first create an oxygen vacancy adjacent to the dissolving TM that would be formed when the produced water leaves the surface and then attach the bidentate ligand, formed from either DEC or EC, to the surface TM. It turns out that bidentate configuration is not stable converging to the monodentate complex with TM at the surface. The estimated adsorption energies of such mono-

dentate complexes with surface Mn are about  $-2.1$  eV for decomposed EC (formed via H-abstraction and ring opening) and only  $-0.6$  eV for decomposed DEC (formed according to the mechanism proposed earlier<sup>11</sup>). We are able to stabilize the bidentate TM complexes only at the later stages of TM dissolution when TM is already in the surface-bound configuration (see the corresponding atomic structures in Figure 4); however, this should not reduce the activation

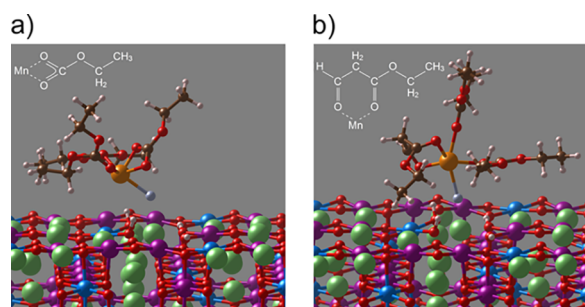


**Figure 4.** Atomic structures of the bidentate  $\beta$ -diketonate Mn complexes with decomposed EC (a) and decomposed DEC (b) fragments upon dissolution. Nondecomposed DEC molecules and fluoride species in the first coordination sphere of Mn are also shown.

barrier significantly. The obtained results indicate that the proposed mechanism is unlikely to lead to substantially reduced activation barriers of TM dissolution, while the experimentally observed diketonate metal complexes from DEC may be formed when TM is already partially dissolved to the surface.

**3.2. TM Dissolution from the Surface-Bound Configuration.** In this section, we consider the next step of TM dissolution at the LNMO surface into the electrolyte through sequential breaking of the two remaining TM–O<sub>2f</sub> bonds starting from the surface-bound configuration shown in Figure 2d. The associated atomic structures along the dissolution pathway for the case with one F<sup>−</sup> are shown in Figure 4, while the barriers are listed in Table 2.

**Table 2. Activation Barriers for Breaking the First ( $\Delta F_2^\ddagger$ ) and Second ( $\Delta F_3^\ddagger$ ) TM–O<sub>2f</sub> Bond (TM = Mn, Ni) in the Surface-Bound Configuration with All Four Oxygen Atoms Adjacent to the Dissolving TMs Being Protonated**

TM	no of F <sup>−</sup>	$\Delta F_2^\ddagger$ (eV)	$\Delta F_3^\ddagger$ (eV)
Mn	1	0.20	1.27
	2	spontaneous	0.52
Ni	1	0.20	1.15
	2	spontaneous	0.30

The free energy barrier for breaking the first TM–O<sub>2f</sub> bond is estimated to be around  $\sim 0.2$  eV (from state a to state b in Figure 5), while the introduction of a second F<sup>−</sup> leads to its spontaneous breaking. Spontaneous bond breaking can also occur through the second protonation of this O<sub>2f</sub> atom that results in the creation of H<sub>2</sub>O. In comparison to the breaking of the first TM–O<sub>2f</sub> bond, the breaking of the second TM–O<sub>2f</sub> bond is energetically expensive, as seen from Table 2. The average free energy barriers to break the last Mn–O<sub>2f</sub> bond are  $\sim 1.3$  eV for 1F<sup>−</sup> and  $\sim 0.5$  eV for 2F<sup>−</sup>, respectively.

**3.3. Correlation between TM Dissolution Barriers and Electrolyte Adsorption Strengths.** Modeling TM dissolu-

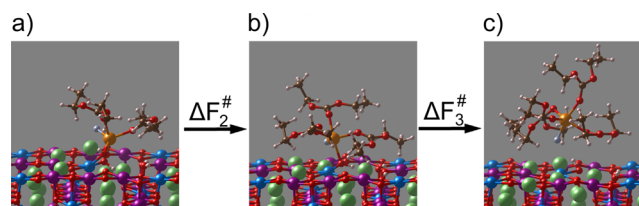


**Figure 5.** Structural snapshots of the initial surface-bound state (a), intermediate state with one TM–O<sub>2f</sub> bond broken (b), and final state with both TM–O<sub>2f</sub> bonds broken (c).

tion reactions at the fully ab initio footing as presented above remains challenging. Although critical mechanistic insights into dissolution dynamics can be obtained using AIMD-based simulations, it is desirable to come up with a simple descriptor that might be used to predict the propensity of a material to dissolve. In this regard, the adsorption energy of the electrolyte species seems to be a natural choice. In the case of CEIs, it is reasonable to expect that stronger adsorption of the electrolyte species will lead to lower dissolution barriers through weakening structural TM–O bonds to alleviate their breaking. Here, we test this correlation on the example of LNMO by plotting dissolution barriers of TMs versus adsorption energies of the electrolyte species (see Figure 6). Adsorption energies

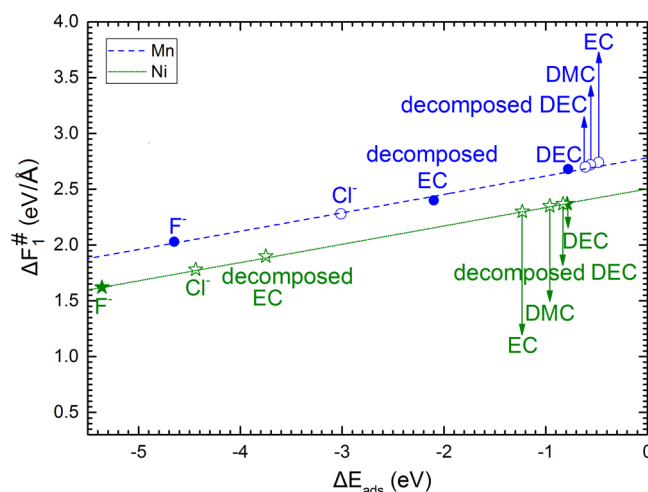


**Figure 6.** Correlation plots between adsorption energies of electrolyte species ( $\Delta E_{\text{ads}}$ ) and TM dissolution barriers ( $\Delta F_1^\ddagger$ ) for Mn (in blue) and Ni (in green). The filled symbols show the calculated values, whereas the open symbols depict predictions of dissolution barriers based on the DFT-computed adsorption energies.

are evaluated from static DFT calculations of single-species adsorption atop the dissolving TM. For simplicity, adsorption energies are estimated without taking into account the difference in solvation free energies because of the difference in the static dielectric constants.<sup>47</sup> Dissolution barriers are estimated for the case when each electrolyte species adsorbed atop TM is embedded in the DEC solution. This means that when the TM dissolves to the surface-bound configuration, it will form additional bond with a DEC molecule from electrolyte, making comparison between different systems more consistent. Also, all the four oxygen atoms at the surface neighboring the dissolving TM are protonated.

The filled symbols in Figure 6 correspond to the cases for which both dissolution barriers and adsorption energies are calculated in this study, whereas the open symbols stand for

predictions of the activation barriers based on computed adsorption energies. It is seen that there is a clear linear relation between adsorption strength and dissolution barriers with  $F^-$  characterized by the lowest (highest) barriers (adsorption energies), followed by  $Cl^-$  and decomposed EC. Nondecomposed organic molecules exhibit weaker adsorption. These results allow one to predict that, for instance, the presence of  $Cl^-$  that may form as a result of  $ClO_4^-$  decomposition should lead to less severe dissolution than in the case of  $F^-$ . Though carried out for the most commonly employed electrolyte species, a similar analysis of adsorption strength can be extended to screen a broader range of electrolyte moieties to predict TM dissolution across various cathode materials.

#### 4. CONCLUSIONS

In this work, we have conducted a systematic analysis of various factors affecting dissolution of TMs (Mn, Ni) from the LNMO spinel cathode based on AIMD free energy calculations. The identified dissolution mechanism qualitatively agrees with previous computational studies of Mn release from the LMO spinel.<sup>12,13</sup> The results show that TM dissolution to the surface-bound state is the rate-limiting step of the overall process with Ni exhibiting slightly smaller dissolution barriers than Mn. Therefore, the larger amounts of dissolved Mn than Ni from LNMO observed experimentally could be attributed to the higher content of Mn at the cathode surface.

The analysis reveals that each of the considered factors—surface protonation, oxygen vacancies, and strongly adsorbed electrolyte species—can significantly lower activation barriers. Our calculations also indicate that the previously hypothesized mechanism of TM dissolution involving chelating  $\beta$ -diketonate species formed upon DEC oxidation at the LNMO surface<sup>11</sup> is unlikely to constitute the primary mechanism of TM dissolution because these species cannot bind strongly to the dissolving TM. Although this may occur at the later stages of dissolution, for instance, by chelating the surface-bound TM, this cannot reduce the overall activation barrier substantially.

By correlating adsorption energies and dissolution barriers, we have also determined a linear relationship between these two quantities, showing that strongly adsorbed species should lead to more facile TM dissolution. This suggests a simple descriptor (adsorption energy) that can be used to predict the propensity of cathode materials to TM dissolution as a function of electrolyte chemistry.

#### AUTHOR INFORMATION

##### Corresponding Author

\*E-mail: valexandrov2@unl.edu. Phone: +1 402 4725323.

##### ORCID

Nadia N. Intan: 0000-0003-1967-178X

Konstantin Klyukin: 0000-0001-8325-8725

Vitaly Alexandrov: 0000-0003-2063-6914

##### Present Address

<sup>†</sup>Konstantin Klyukin, Department of Materials Science and Engineering, Massachusetts Institute of Technology, 77 Massachusetts Avenue, Cambridge, MA, 02139, USA.

##### Notes

The authors declare no competing financial interest.

#### ACKNOWLEDGMENTS

This research used resources of the National Energy Research Scientific Computing Center, a DOE Office of Science User Facility supported by the Office of Science of the U.S. Department of Energy under contract no. DE-AC02-05CH1123. We also acknowledge Extreme Science and Engineering Discovery Environment (XSEDE),<sup>48</sup> which is supported by National Science Foundation grant number ACI-1548562, and the Holland Computing Center of the University of Nebraska, which receives support from the Nebraska Research Initiative for providing computational resources. V.A. is grateful for financial support from the startup package provided by the University of Nebraska—Lincoln.

#### REFERENCES

- (1) Amatucci, G.; Tarascon, J.; Klein, L. Cobalt Dissolution in  $LiCoO_2$ -based Non-Aqueous Rechargeable Batteries. *Solid State Ionics* **1996**, *83*, 167–173.
- (2) Striebel, K.; Shim, J.; Sierra, A.; Yang, H.; Song, X.; Kostecki, R.; McCarthy, K. The Development of Low Cost  $LiFePO_4$ -Based High Power Lithium-Ion Batteries. *J. Power Sources* **2005**, *146*, 33–38.
- (3) Xiao, X.; Ahn, D.; Liu, Z.; Kim, J.-H.; Lu, P. Atomic Layer Coating to Mitigate Capacity Fading Associated with Manganese Dissolution in Lithium Ion Batteries. *Electrochem. Commun.* **2013**, *32*, 31–34.
- (4) Pieczonka, N. P. W.; Liu, Z.; Lu, P.; Olson, K. L.; Moote, J.; Powell, B. R.; Kim, J.-H. Understanding Transition-Metal Dissolution Behavior in  $LiMn_{1.5}Ni_{0.5}O_4$  High-Voltage Spinel for Lithium Ion Batteries. *J. Phys. Chem. C* **2013**, *117*, 15947–15957.
- (5) Gilbert, J. A.; Bareño, J.; Spila, T.; Trask, S. E.; Miller, D. J.; Polzin, B. J.; Jansen, A. N.; Abraham, D. P. Transition Metal Dissolution, Ion Migration, Electrocatalytic Reduction and Capacity Loss in Lithium-Ion Full Cells. *J. Electrochem. Soc.* **2017**, *164*, A389–A399.
- (6) Ma, J.; Hu, P.; Cui, G.; Chen, L. Surface and Interface Issues in Spinel  $LiNi_{0.5}Mn_{1.5}O_4$ : Insights into a Potential Cathode Material for High Energy Density Lithium Ion Batteries. *Chem. Mater.* **2016**, *28*, 3578–3606.
- (7) Ariyoshi, K.; Iwakoshi, Y.; Nakayama, N.; Ohzuku, T. Topotactic Two-Phase Reactions of  $Li[Ni_{1/2}Mn_{3/2}]O_4$  (P4<sub>3</sub>2) in Nonaqueous Lithium Cells. *J. Electrochem. Soc.* **2004**, *151*, A296–A303.
- (8) Börner, M.; Niehoff, P.; Vortmann, B.; Nowak, S.; Winter, M.; Schappacher, F. M. Comparison of Different Synthesis Methods for  $LiNi_{0.5}Mn_{1.5}O_4$  Influence on Battery Cycling Performance, Degradation, and Aging. *Energy Technol.* **2016**, *4*, 1631–1640.
- (9) Shilina, Y.; Ziv, B.; Meir, A.; Banerjee, A.; Ruthstein, S.; Luski, S.; Aurbach, D.; Halalay, I. C. Combined Electron Paramagnetic Resonance and Atomic Absorption Spectroscopy/Inductively Coupled Plasma Analysis As Diagnostics for Soluble Manganese Species from Mn-Based Positive Electrode Materials in Li-ion Cells. *Anal. Chem.* **2016**, *88*, 4440–4447.
- (10) Qiao, R.; Wang, Y.; Olalde-Velasco, P.; Li, H.; Hu, Y.-S.; Yang, W. Direct Evidence of Gradient Mn (II) Evolution at Charged States in  $LiNi_{0.5}Mn_{1.5}O_4$  Electrodes with Capacity Fading. *J. Power Sources* **2015**, *273*, 1120–1126.
- (11) Jarry, A.; Gottis, S.; Yu, Y.-S.; Roque-Rosell, J.; Kim, C.; Cabana, J.; Kerr, J.; Kostecki, R. The Formation Mechanism of Fluorescent Metal Complexes at the  $Li_xNi_{0.5}Mn_{1.5}O_{4-\delta}$  Carbonate Ester Electrolyte Interface. *J. Am. Chem. Soc.* **2015**, *137*, 3533–3539.
- (12) Benedek, R. Role of Disproportionation in the Dissolution of Mn from Lithium Manganate Spinel. *J. Phys. Chem. C* **2017**, *121*, 22049–22053.
- (13) Leung, K. First-Principles Modeling of Mn (II) Migration above and Dissolution from  $Li_xMn_2O_4$  (001) Surfaces. *Chem. Mater.* **2016**, *29*, 2550–2562.

- (14) Leung, K. First-Principles Modeling of the Initial Stages of Organic Solvent Decomposition on  $\text{Li}_x\text{Mn}_2\text{O}_4$  (100) Surfaces. *J. Phys. Chem. C* **2012**, *116*, 9852–9861.
- (15) Kumar, N.; Leung, K.; Siegel, D. J. Crystal Surface and State of Charge Dependencies of Electrolyte Decomposition on  $\text{LiMn}_2\text{O}_4$  Cathode. *J. Electrochem. Soc.* **2014**, *161*, E3059–E3065.
- (16) Sushko, P. V.; Rosso, K. M.; Zhang, J.-G.; Liu, J.; Sushko, M. L. Oxygen Vacancies and Ordering of d-levels Control Voltage Suppression in Oxide Cathodes: the Case of Spinel  $\text{LiNi}_{0.5}\text{Mn}_{1.5}\text{O}_{4-\delta}$ . *Adv. Funct. Mater.* **2013**, *23*, 5530–5535.
- (17) Shiiba, H.; Zetsu, N.; Nakayama, M.; Oishi, S.; Teshima, K. Defect Formation Energy in Spinel  $\text{LiNi}_{0.5}\text{Mn}_{1.5}\text{O}_4$  - $\delta$  Using Ab Initio DFT Calculations. *J. Phys. Chem. C* **2015**, *119*, 9117–9124.
- (18) Chen, Y.; Sun, Y.; Huang, X. Origin of the Ni/Mn Ordering in High-Voltage Spinel  $\text{LiMn}_{1.5}\text{Ni}_{0.5}\text{O}_4$ : The Role of Oxygen Vacancies and Cation Doping. *Comput. Mater. Sci.* **2016**, *115*, 109–116.
- (19) Yi, T.-F.; Xie, Y.; Ye, M.-F.; Jiang, L.-J.; Zhu, R.-S.; Zhu, Y.-R. Recent Developments in the Doping of  $\text{LiNi}_{0.5}\text{Mn}_{1.5}\text{O}_4$  Cathode Material for 5 V Lithium-Ion Batteries. *Ionics* **2011**, *17*, 383–389.
- (20) Kim, S.; Aykol, M.; Wolverton, C. Surface Phase Diagram and Stability of (001) and (111)  $\text{LiMn}_2\text{O}_4$  Spinel Oxides. *Phys. Rev. B: Condens. Matter Mater. Phys.* **2015**, *92*, 115411.
- (21) Lee, E.; Persson, K. A. First-Principles Study of the Nano-Scaling Effect on the Electrochemical Behavior in  $\text{LiNi}_{0.5}\text{Mn}_{1.5}\text{O}_4$ . *Nanotechnology* **2013**, *24*, 424007.
- (22) Lee, E.; Persson, K. A. Corrigendum: First-Principles Study of the Nano-Scaling Effect on the Electrochemical Behavior in  $\text{LiNi}_{0.5}\text{Mn}_{1.5}\text{O}_4$ . *Nanotechnology* **2014**, *25*, 159501.
- (23) Shi, J.; Wang, Z.; Fu, Y. Q. Density Functional Theory Analysis of Surface Structures of Spinel  $\text{LiNi}_{0.5}\text{Mn}_{1.5}\text{O}_4$  Cathode Materials. *J. Mater. Sci.* **2017**, *52*, 605–612.
- (24) Intan, N. N.; Klyukin, K.; Alexandrov, V. Theoretical Insights into Oxidation States of Transition Metals at (001) and (111)  $\text{LiNi}_{0.5}\text{Mn}_{1.5}\text{O}_4$  Spinel Surfaces. *J. Electrochem. Soc.* **2018**, *165*, A1099–A1103.
- (25) Kresse, G.; Furthmüller, J. Efficiency of Ab-Initio Total Energy Calculations for Metals and Semiconductors Using a Plane-Wave Basis Set. *Comput. Mater. Sci.* **1996**, *6*, 15–50.
- (26) Kresse, G.; Furthmüller, J. Efficient iterative schemes for ab initio total-energy calculations using a plane-wave basis set. *Phys. Rev. B: Condens. Matter Mater. Phys.* **1996**, *54*, 11169.
- (27) Blöchl, P. E. Projector Augmented-Wave Method. *Phys. Rev. B: Condens. Matter Mater. Phys.* **1994**, *50*, 17953.
- (28) Burke, K.; Perdew, J.; Ernzerhof, M. Generalized Gradient Approximation Made Simple. *Phys. Rev. Lett.* **1997**, *78*, 1396.
- (29) Perdew, J. P.; Ruzsinszky, A.; Csonka, G. I.; Vydrov, O. A.; Scuseria, G. E.; Constantin, L. A.; Zhou, X.; Burke, K. Restoring the Density-Gradient Expansion for Exchange in Solids and Surfaces. *Phys. Rev. Lett.* **2008**, *100*, 136406.
- (30) Grimme, S.; Antony, J.; Ehrlich, S.; Krieg, H. A Consistent and Accurate Ab Initio Parametrization of Density Functional Dispersion Correction (DFT-D) for the 94 Elements H–Pu. *J. Chem. Phys.* **2010**, *132*, 154104.
- (31) Biškup, N.; Martínez, J.; Arroyo y de Dompablo, M.; Díaz-Carrasco, P.; Morales, J. Relation Between the Magnetic Properties and the Crystal and Electronic Structures of Manganese Spinels  $\text{LiNi}_{0.5}\text{Mn}_{1.5}\text{O}_4$  and  $\text{LiCu}_{0.5}\text{Mn}_{1.5}\text{O}_{4-\delta}$  ( $0 \leq \delta \leq 0.125$ ). *J. Appl. Phys.* **2006**, *100*, 093908.
- (32) Amdouni, N.; Zaghbi, K.; Gendron, F.; Mauger, A.; Julien, C. M. Magnetic Properties of  $\text{LiNi}_{0.5}\text{Mn}_{1.5}\text{O}_4$  Spinels Prepared by Wet Chemical Methods. *J. Magn. Magn. Mater.* **2007**, *309*, 100–105.
- (33) Yu, H.; Qian, Y.; Otani, M.; Tang, D.; Guo, S.; Zhu, Y.; Zhou, H. Study of the Lithium/Nickel Ions Exchange in the Layered  $\text{LiNi}_{0.42}\text{Mn}_{0.42}\text{Co}_{0.16}\text{O}_2$  Cathode Material for Lithium Ion Batteries: Experimental and First-Principles Calculations. *Energy Environ. Sci.* **2014**, *7*, 1068–1078.
- (34) Nosé, S. A Molecular Dynamics Method for Simulations in the Canonical Ensemble. *Mol. Phys.* **1984**, *52*, 255–268.
- (35) Hoover, W. G. Canonical Dynamics: Equilibrium Phase-Space Distributions. *Phys. Rev. A: At, Mol., Opt. Phys.* **1985**, *31*, 1695.
- (36) Straatsma, T. P.; Berendsen, H. J. C.; Postma, J. P. M. Free Energy of Hydrophobic Hydration: A Molecular Dynamics Study of Noble Gases in Water. *J. Chem. Phys.* **1986**, *85*, 6720–6727.
- (37) Benedek, R.; Thackeray, M. M.; Low, J.; Bučko, T. Simulation of Aqueous Dissolution of Lithium Manganate Spinel from First Principles. *J. Phys. Chem. C* **2012**, *116*, 4050–4059.
- (38) Bucko, T. Ab Initio Calculations of Free-Energy Reaction Barriers. *J. Phys.: Condens. Matter* **2008**, *20*, 064211. DOI: 10.1088/0953-8984/20/6/064211
- (39) Klyukin, K.; Rosso, K. M.; Alexandrov, V. Iron Dissolution from Goethite ( $\alpha\text{-FeOOH}$ ) Surfaces in Water by Ab Initio Enhanced Free-Energy Simulations. *J. Phys. Chem. C* **2018**, *122*, 16086–16091.
- (40) Wang, H.; Xie, X.; Wei, X.; Zhang, X.; Zhang, J.; Huang, Y.; Li, Q. A New Strategy to Stabilize Capacity and Insight into the Interface Behavior in Electrochemical Reaction of  $\text{LiNi}_{0.5}\text{Mn}_{1.5}\text{O}_4$ /Graphite System for High-Voltage Lithium-Ion Batteries. *ACS Appl. Mater. Interfaces* **2017**, *9*, 33274–33287.
- (41) Yamane, H.; Inoue, T.; Fujita, M.; Sano, M. A Causal Study of the Capacity Fading of  $\text{Li}_{1.01}\text{Mn}_{1.99}\text{O}_4$  Cathode at 80 °C, and the Suppressing Substances of its Fading. *J. Power Sources* **2001**, *99*, 60–65.
- (42) Du Pasquier, A.; Blyr, A.; Courjal, P.; Larcher, D.; Amatucci, G.; Gerand, B.; Tarascon, J.-M. Mechanism for Limited 55 C Storage Performance of  $\text{Li}_{1.05}\text{Mn}_{1.95}\text{O}_4$  Electrodes. *J. Electrochem. Soc.* **1999**, *146*, 428–436.
- (43) Fu, M. H.; Huang, K. L.; Liu, S. Q.; Liu, J. S.; Li, Y. K. Lithium Difluoro(oxalato)borate/Ethylene Carbonate + Propylene Carbonate + Ethyl (Methyl) Carbonate Electrolyte for  $\text{LiMn}_2\text{O}_4$  Cathode. *J. Power Sources* **2010**, *195*, 862–866.
- (44) Gallus, D. R.; Schmitz, R.; Wagner, R.; Hoffmann, B.; Nowak, S.; Cekic-Laskovic, I.; Schmitz, R. W.; Winter, M. The Influence of Different Conducting Salts on the Metal Dissolution and Capacity Fading of NCM Cathode Material. *Electrochim. Acta* **2014**, *134*, 393–398.
- (45) Sloop, S. E.; Pugh, J. K.; Wang, S.; Kerr, J. B.; Kinoshita, K. Chemical Reactivity of  $\text{PF}_5$  and  $\text{LiPF}_6$  in Ethylene Carbonate/Dimethyl Carbonate Solutions. *Electrochem. Solid-State Lett.* **2001**, *4*, A42–A44.
- (46) Kawamura, T.; Okada, S.; Yamaki, J.-i. Decomposition reaction of  $\text{LiPF}_6$ -based electrolytes for lithium ion cells. *J. Power Sources* **2006**, *156*, S47–S54.
- (47) Xu, K. Nonaqueous Liquid Electrolytes for Lithium-Based Rechargeable Batteries. *Chem. Rev.* **2004**, *104*, 4303–4418.
- (48) Towns, J.; Cockerill, T.; Dahan, M.; Foster, I.; Gaither, K.; Grimshaw, A.; Hazlewood, V.; Lathrop, S.; Lifka, D.; Peterson, G. D.; Roskies, R.; Scott, J. R.; Wilkins-Diehr, N. XSEDE: Accelerating Scientific Discovery. *Comput. Sci. Eng.* **2014**, *16*, 62–74.